Research Square

Preprints are preliminary reports that have not undergone peer review.
They should not be considered conclusive, used to inform clinical practice,
or referenced by the media as validated information.

Multistage dolomitizing fluids and their constraints on reservoir quality in the Ediacaran Dengying Formation, Sichuan Basin

Qiufen Li
Research Institute of Petroleum Exploration and Development
Cong Tan
340330888@qq.com
Research Institute of Petroleum Exploration and Development
Tongshan Wang
Research Institute of Petroleum Exploration and Development
Qiuding Du
Southwest Petroleum University
Zhidong Gu
Research Institute of Petroleum Exploration and Development
Shuyuan Shi
Research Institute of Petroleum Exploration and Development
Xiufen Zhai
Research Institute of Petroleum Exploration and Development

Research Article

Keywords: Dolomitization fluid diversity, high-quality reservoirs, Dengying Formation, Ediacaran, Sichuan Basin

Posted Date: November 25th, 2026

DOI: https://doi.org/10.21203/rs.3.rs-11796958/v1

License: This work is licensed under a Creative Commons Attribution 4.0 International License.
Read Full License

Additional Declarations: No competing interests reported.

Multistage dolomitizing fluids and their constraints on reservoir quality in the Ediacaran Dengying Formation, Sichuan Basin

Li Qiufen[a], Tan Cong[a*], Wang Tongshan[a], Du Qiuding[b], Gu Zhidong[a], Shi Shuyuan[a], Zhai Xiufen[a]

[a]Research Institute of Petroleum Exploration & Development, PetroChina, Beijing 100083, China

[b]School of Geoscience and Technology, Southwest Petroleum University, Chengdu 610500, China

* Corresponding author. E-mail: 340330888@qq.com

Abstract: The Ediacaran Dengying Formation in the Sichuan Basin hosts deeply buried dolomite reservoirs with significant exploration potential. However, the multistage fluid evolution and its differential control on reservoir quality remain poorly constrained. This study integrates petrography, in situ C–O isotopes and bulk Sr isotopes, trace elements, and fluid inclusion microthermometry on dolomites from the fourth member of the Dengying Formation in the northern Sichuan Basin. Four diagenetic stages are recognized across seven dolomite types, each recording distinct diagenetic fluids: (1) matrix and fibrous/foliated cements precipitated from evaporative seawater during penecontemporaneous–early diagenesis; (2) fine-crystalline dolomite formed from modified seawater in shallow burial; (3) medium- to coarse-crystalline dolomite precipitated from formation waters in medium-to-deep burial; and (4) saddle dolomite and associated quartz record tectonically driven hydrothermal fluids. Reservoir quality is primarily controlled by the interplay of sedimentary facies, early dolomitization, and late diagenetic modification. Microbial mound-shoal complexes with early dolomitization provide the primary framework for high-quality reservoirs in the northern Sichuan Basin, whereas hydrothermal alteration locally enhances reservoir quality, as documented in the Gaomo area. This study establishes a facies–diagenesis–fluid ternary model for reservoir prediction in deeply buried dolomites.

Keywords: Dolomitization fluid diversity, high-quality reservoirs, Dengying Formation, Ediacaran, Sichuan Basin

1. Introduction

Ultradeep carbonate rocks in China's sedimentary basins contain abundant oil and gas resources (Pang et al. 2020; Ma et al. 2022; Jia and Zhang 2023). Several large to superlarge fields have been discovered, including Puguang, Anyue, Shunbei and Fuman (Ma et al. 2007; Du et al. 2014; Ma et al. 2022; Yang et al. 2022; Han et al. 2023), and ultradeep carbonates have thus become a major frontier for oil and gas exploration in China.

With the advance of exploration, cores from deeply buried strata show that the porosity of deep to ultradeep carbonates, and of dolomites in particular, does not correlate systematically with burial depth, and that high-quality reservoirs still develop at ultradeep depths. The formation of such reservoirs is nevertheless complex, and the sedimentary environment together with early diagenetic karstification are regarded as the main controlling factors (Bjørlykke and Jahren 2012; Shen et al. 2016; Zhao et al. 2022a). Some authors argue that late diagenesis, epigenetic dissolution and hydrothermal processes can substantially improve reservoir properties (Zhao et al. 2012; Cai et al. 2014; Jiang et al. 2018), whereas Ma et al. (2010) attributed the origin of deep high-quality dolomite reservoirs to the combined control of sedimentation, diagenesis and tectonics. Despite this progress, two critical issues remain unresolved for the Dengying Formation in the northern Sichuan Basin. First, the genetic link between the diverse dolomite types and their parent fluids has not been established systematically, so that interpretations of the diagenetic evolution remain conflicting. Second, the relative contributions of early microbial dolomitization and late hydrothermal alteration to reservoir quality are still debated, which hampers targeted exploration.

The Ediacaran Dengying Formation in the Sichuan Basin hosts a suite of deeply buried, high-quality dolomite reservoirs. Its dolomites have experienced deep burial, multistage tectonic alteration and complex fluid evolution, and the origins of the reservoirs are correspondingly diverse. The main mechanisms proposed are (1) dissolution by meteoric freshwater during tectonic uplift (Luo et al. 2017; Wang 2019; Li et al. 2022), (2) dissolution and reworking by burial organic acids, and (3) dissolution related to deep hydrothermal fluid activity (Feng et al. 2017; Li et al. 2019). These processes controlled both the modification of the Dengying dolomites and the

formation of high-quality reservoirs.

The Dengying Formation contains a great variety of dolomite types, and these differences record the relationships between dolomitizing fluids and formation environments: no single dolomitization mechanism can account for all of the dolomite in the basin. Diagenetic environments and post-depositional fluids modify the texture, mineralogy, elemental composition and isotopic signature of carbonate rocks (Swart 2015), so geochemical tracers such as trace elements and the stable ^{13}C and ^{18}O isotopes, combined with petrography, are used to identify and reconstruct diagenetic environments and processes (Zhao and Zheng 2017; Javanbakht et al. 2018).

Understanding how these reservoirs formed during dolomite sedimentation and diagenesis is therefore essential for improving reservoir evaluation in the study area. Here the fourth member of the Dengying Formation at the Hujiaba section on the northern margin of the Sichuan Basin is taken as a case study, and the reservoirs are investigated using petrography, carbon–oxygen–strontium isotope geochemistry, element geochemistry and fluid inclusion data. Together with the supporting petrological and mineralogical evidence, the aims are to identify the diagenetic environments, reconstruct the diagenetic pore-evolution pathway, and evaluate the formation and preservation mechanisms of high-quality reservoirs, thereby providing a sedimentological and diagenetic basis for predicting exploration targets in the area.

2. Geological setting

In the northwestern part of the Yangtze plate, the Sichuan Basin is a superimposed basin developed on the Yangtze craton. It is a NE–SW-trending rhombus, bounded to the west by the Songpan–Garze orogenic belt and to the north by the Qinling–Dabie orogenic belt (Liu et al. 2021; Fig. 1a, b). The Yangtze plate entered the marine cratonic stage in the Ediacaran. From the late Ediacaran to the early Cambrian, rifting associated with the Xingkai tectonic movement developed in the middle and upper Yangtze plate and controlled the Ediacaran depressions of the Sichuan Basin (Luo 1991). Judging from the Early Cambrian palaeogeography, deposition of the upper Ediacaran Dengying Formation took place on an alternating trough-and-platform palaeogeography that was elevated in the west and low in the east (Wen et al. 2021).

The Dengying Formation (551–541 Ma) belongs to the Ediacaran. It records the marine sedimentary response to global warming after the end of the Nanhua glaciation and contains skeletal remains documenting the evolution of early animals immediately before the Cambrian explosion (Zhu et al. 2007; Ding et al. 2021). Microbial mound-shoal complexes composed largely of microbial dolomite are an important exploration target in the deep ancient carbonates of the Sichuan Basin (Zhao et al. 2022b; Yang et al. 2022). The rocks consist mainly of grain dolomite, microbial dolomite and a distinctive grape-like dolomite. Lithologically the formation is divided into four members, from bottom to top (Deng et al. 2015): the Deng 1 member consists of algal-mud and microcrystalline dolomite; the Deng 2 member is dominated by thick microbial dolomite; the Deng 3 member consists of terrestrial clastic deposits; and the Deng 4 member is dominated by microbial and crystalline dolomite, with local silicified laminae and siliceous bands (Fig. 1c).

Deposition of the Dengying Formation in the Sichuan Basin took place on a large carbonate platform (Liu and Xu 1994). The discovery of the Deyang–Anyue rift trough in the basin (Li et al. 2015; Wei et al. 2015; Du et al. 2016) overturned the earlier view of a monolithic craton interior. The Dengying Formation is accordingly interpreted in a rimmed-platform model, comprising slope–basin, platform-margin (mounds and shoals) and restricted platform (tidal flat, lagoon, intraplatform mound-shoal) facies (Wei et al. 2018).

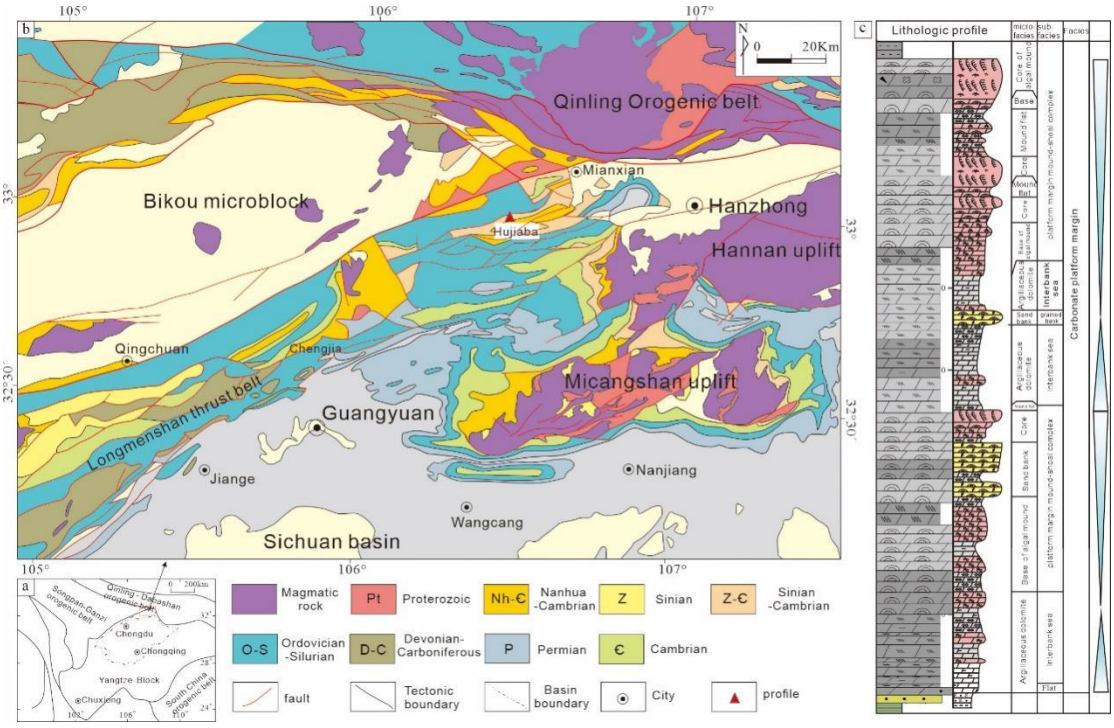


Fig. 1 Geological setting of the study area. (a) Tectonic setting of South China and location of the middle-upper Yangtze area. (b) Geological map of northeastern Sichuan region showing the location and geological setting of the deposits. (c) Stratigraphic column and lithofacies interpretation of the fourth member of the Dengying Formation in the Hujiaba section.

3. Materials and methods

Dolomite samples for this study were collected from the fourth member of the Dengying Formation at the Hujiaba section on the northern margin of the Sichuan Basin. Petrographic examination identified seven dolomite types: matrix dolomite, fibrous rim cement, foliated cement, fine-crystalline cement, medium-crystalline cement, coarse-crystalline cement and saddle dolomite. These samples were analysed for rare earth elements (Table 1) and for major and trace elements (Fig. 2); carbon and oxygen isotope analyses were performed on 34 samples, including parallel powder analyses of the laser-ablation positions (Table 2), and strontium isotope analyses on 20 samples (Table 3).

Petrographic examination was carried out on polished thin sections under a polarizing microscope. Cathodoluminescence (CL) imaging of the same thin sections

was used to distinguish primary from burial cements, to determine the growth zonation of the dolomites and to establish the paragenetic sequence presented in Section 5.1.

Major and trace element and rare earth element analyses were carried out at the PetroChina Hangzhou Research Institute of Geology. Analyses used an Australian Scientific Instruments (ASI) RESOlution-SE laser ablation–inductively coupled plasma–mass spectrometer, with an analytical precision better than 1%. Reference materials were NIST 610, NIST 612, NIST 614 and MACS-3. Rare earth element concentrations were normalized to the Post-Archean Australian Shale (PAAS) composition of Pourmand et al. (2012).

Carbon and oxygen isotope analyses were performed at the PetroChina Hangzhou Research Institute of Geology. A laser ablation isotope ratio mass spectrometry (LA-IRMS) system was used for real-time in situ analysis, with a spot size of 20 μm and a working current of 14–20 A; the analytical precision was better than 0.01‰ for $\delta^{13}C$ and 0.02‰ for $\delta^{18}O$. Powder samples were additionally microdrilled at the same positions as the laser pits so that the two methods could be compared directly; the powders were analysed on a Delta V Advantage isotope ratio mass spectrometer at 27 °C and 49% relative humidity. Reference materials were GBW04405 and the internal standard 811, and results are reported in per mil (‰) relative to Vienna Peedee Belemnite (VPDB).

Strontium isotope analyses were performed on 20 dolomite samples at the PetroChina Hangzhou Research Institute of Geology using a Triton Plus thermal ionization mass spectrometer. Samples were loaded on a single Ta filament and ionized at 1450 °C. The reproducibility (2σ) was 0.000010–0.000027. Reference materials were JDO-1, BHVO-1 and BCR, and results are reported as $^{87}Sr/^{86}Sr$ ratios.

Fluid inclusion microthermometry was carried out on the different dolomite types that fill dissolution pores and cavities of the fourth member at the National Experimental Teaching Demonstration Center for Oil and Gas Geology and Exploration, Southwest Petroleum University. A Linkam THMS 600 heating–freezing stage mounted on a DM2500P fluorescence microscope was used. Heating and cooling rates were 1–5 °C/min, and the calibration error was ±1 °C.

4. Results

4.1 Trace elements

The Mn and Fe contents of matrix dolomite and of the different generations of dolomite cement from the northern Sichuan Basin are shown in Fig. 2, and their Sr contents in Fig. 5b.

Matrix dolomites contain 0.17–11.18 ppm Sr (avg. 5.32 ppm), 1.40–155.9 ppm Mn (avg. 32.60 ppm) and 22.93–315.4 ppm Fe (avg. 97.44 ppm).

Fibrous rim dolomites contain 3.79–4.35 ppm Sr (avg. 4.11 ppm), 8.04–103.8 ppm Mn (avg. 41.03 ppm) and 69.46–82.25 ppm Fe (avg. 73.94 ppm).

Foliated dolomites contain 5.31–7.64 ppm Sr (avg. 6.54 ppm), 3.03–7.05 ppm Mn (avg. 4.93 ppm) and 69.86–88.12 ppm Fe (avg. 78.71 ppm).

Fine-crystalline dolomites contain 1.10–11.16 ppm Sr (avg. 5.71 ppm), 6.28–188.7 ppm Mn (avg. 64.51 ppm) and 68.8–127.2 ppm Fe (avg. 99.48 ppm).

Medium-crystalline dolomites contain 3.95–8.68 ppm Sr, 26.92–197.1 ppm Mn (avg. 87.73 ppm) and 52.62–138.1 ppm Fe (avg. 75.14 ppm).

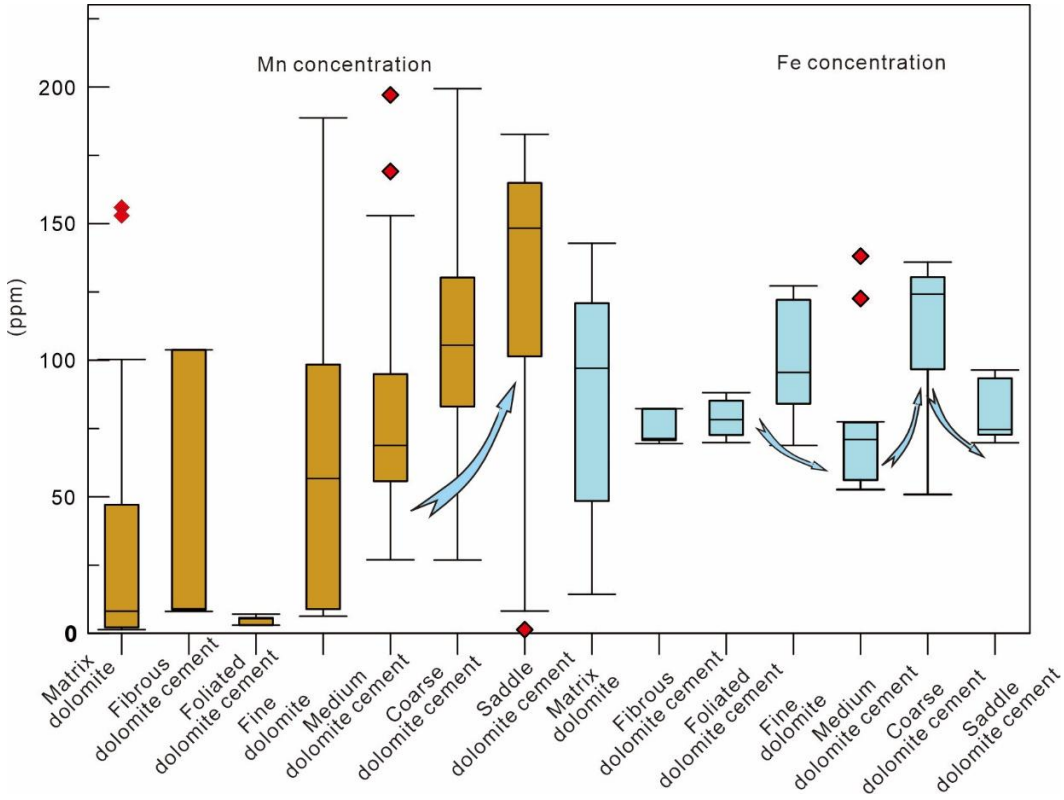


Fig. 2 Box plot showing the distributions of Fe and Mn concentrations of matrix dolomite and dolomite cements in the Ediacaran Dengying Formation.

Compared with the matrix dolomite and the fibrous and foliated cements, the fine- and medium-crystalline cements show a progressive increase in Mn content to values markedly higher than those of the host rocks, whereas Fe contents remain broadly similar. This trend records increasingly reducing pore-water conditions with progressive burial.

Coarse-crystalline dolomite occurs as cement in secondary pores and contains 4.97–24.28 ppm Sr (avg. 18.97 ppm), 26.85–199.4 ppm Mn (avg. 104.13 ppm) and 50.81–135.9 ppm Fe (avg. 106.85 ppm).

Saddle dolomite, also termed baroque dolomite, is characterized by curved crystal faces, spear-shaped terminations and undulose extinction. It contains 3.85–43.57 ppm Sr (avg. 9.46 ppm), 8.17–182.7 ppm Mn (avg. 119.18 ppm) and 69.77–96.42 ppm Fe (avg. 80.09 ppm).

4.2 REEs

The rare earth element (REE) compositions of matrix dolomite and of the different generations of dolomite cement are shown in Fig. 3 and listed in Table 1. All values are normalized to PAAS.

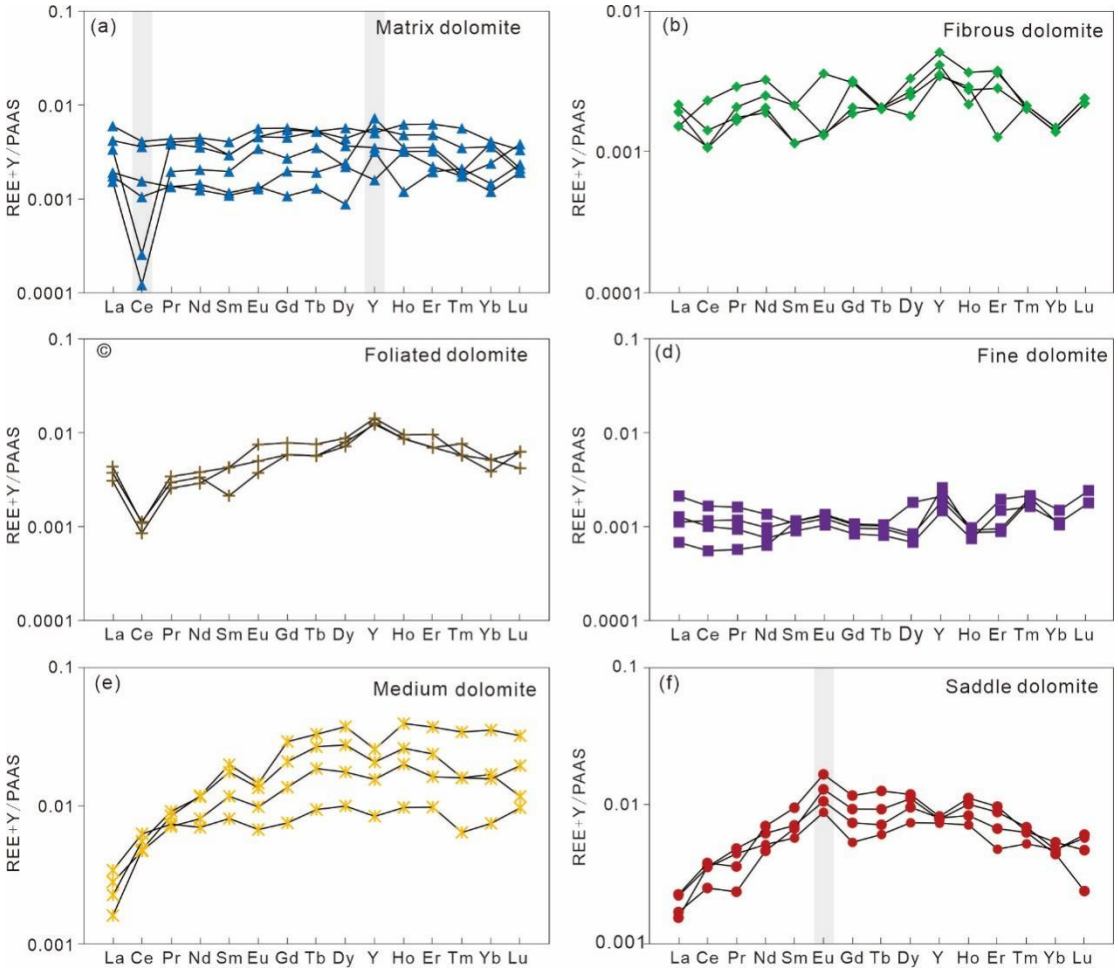


Fig. 3 Rare earth element distribution patterns for matrix dolomite and dolomite cements of the Ediacaran Dengying Formation.

Post-Archean Australian Shale (PAAS) normalized REE patterns of the Dengying Formation dolomite and its diagenetic cements (PAAS values from Pourmand et al. 2012).

Table 1 REEs of matrix dolomite and dolomite cements of the Ediacaran Dengying Formation.

Sample No.	Rock type	Element (ppm)																		
		La	Ce	Pr	Nd	Sm	Eu	Gd	Tb	Dy	Y	Ho	Er	Tm	Yb	Lu	ΣREE+Y	LREE/HREE	δCe	δEu
1	Matrix dolomite	6.01	4.10	4.36	4.47	4.07	5.64	5.68	5.25	5.71	5.06	6.23	6.26	5.66	4.12	3.32	75.94	0.61	0.79	1.16
2	Matrix dolomite	4.19	3.60	3.84	3.56	2.94	4.59	5.43	5.26	4.41	5.70	4.81	4.84	3.50	3.59	1.92	62.18	0.58	0.90	1.10
3	Matrix dolomite	1.91	1.55	1.35	1.44	1.16	1.35	1.07	1.30	0.88	3.19	1.20	1.95	2.10	1.46	2.33	24.24	0.57	0.95	1.21
4	Matrix dolomite	1.75	1.05	1.37	1.24	1.09	1.27	1.98	1.92	2.42	7.28	3.51	3.53	1.94	3.93	2.12	36.39	0.27	0.68	0.83
5	Matrix dolomite	3.38	0.26	4.01	4.24	2.94	4.59	4.52	5.26	3.67	3.52	3.21	3.22	1.75	2.39	3.83	50.80	0.62	0.07	1.23
6	Matrix dolomite	1.53	0.12	1.96	2.05	1.96	3.44	2.72	3.50	2.20	1.59	3.21	2.22	1.75	1.20	1.92	31.38	0.55	0.07	1.47
7	Fibrous dolomite cement	1.52	2.33	2.92	3.27	2.14	3.62	3.12	2.02	3.35	5.13	3.69	3.79	2.03	1.39	2.21	42.53	0.59	1.05	1.38
8	Fibrous dolomite cement	1.53	1.09	2.09	2.53	2.14	1.32	2.08	2.02	2.51	3.56	2.77	2.84	2.03	1.39	2.21	32.10	0.50	0.60	0.62
9	Fibrous dolomite cement	2.17	1.43	1.76	1.90	1.15	1.34	3.22	2.08	2.71	4.17	2.18	3.66	2.13	1.49	2.41	33.82	0.41	0.72	0.61
10	Fibrous dolomite cement	1.93	1.07	1.66	2.06	1.15	1.34	1.88	2.08	1.81	3.48	2.91	1.28	2.13	1.49	2.41	28.69	0.47	0.60	0.89
11	Foliated dolomite cement	3.07	0.85	2.56	2.88	4.26	4.98	5.82	5.66	7.13	12.63	8.61	6.95	5.72	5.14	6.25	82.51	0.29	0.30	0.99
12	Foliated dolomite cement	4.34	1.09	3.41	3.79	4.26	7.47	7.76	7.55	8.72	14.20	9.48	9.55	5.72	3.85	6.25	97.45	0.33	0.28	1.24
13	Foliated dolomite cement	3.75	1.12	2.94	3.34	2.13	3.73	5.82	5.66	7.93	12.28	8.61	6.95	7.62	5.14	4.17	81.19	0.27	0.33	0.94
14	Fine-crystalline dolomite cement	1.27	1.00	0.94	0.75	0.90	1.04	0.83	0.80	0.68	1.47	0.74	1.48	1.63	1.10	1.78	16.43	0.56	0.91	1.20
15	Fine-crystalline dolomite cement	2.11	1.65	1.61	1.35	1.06	1.22	0.96	0.94	0.78	2.60	0.87	0.88	1.92	0.00	0.00	17.93	1.01	0.89	1.20
16	Fine-crystalline dolomite cement	0.68	0.55	0.57	0.63	1.14	1.32	1.04	1.01	0.84	1.87	0.92	0.95	2.03	1.04	0.00	14.59	0.50	0.89	1.21
17	Fine-crystalline dolomite cement	1.12	1.15	1.17	0.97	1.15	1.34	1.07	1.04	1.81	2.11	0.97	1.95	2.13	1.49	2.41	21.90	0.46	1.01	1.21
18	Medium-crystalline dolomite cement	1.60	4.80	8.44	11.82	19.84	14.52	29.12	32.93	37.35	25.67	39.37	37.07	34.17	35.33	32.12	364.16	0.20	0.95	0.59
19	Medium-crystalline dolomite cement	2.80	4.69	7.07	8.07	11.70	9.80	13.60	18.57	17.52	15.51	19.98	16.19	15.92	16.84	11.69	189.94	0.30	0.95	0.77

20	Medium-crystalline dolomite cement	2.25	5.52	9.10	11.59	17.55	13.45	20.87	26.73	27.51	20.69	26.03	23.67	15.92	15.64	19.48	255.99	0.30	0.97	0.70
21	Medium-crystalline dolomite cement	3.41	6.25	7.34	6.96	8.07	6.71	7.51	9.37	9.95	8.37	9.71	9.76	6.40	7.45	9.64	116.91	0.55	1.16	0.86
22	Saddle dolomite cement	2.28	3.87	3.62	7.13	9.67	16.84	11.83	12.80	12.09	8.35	11.37	9.85	6.52	5.44	4.77	126.43	0.52	1.31	1.57
23	Saddle dolomite cement	1.70	2.56	2.38	4.71	6.85	13.14	9.46	9.43	11.25	8.01	10.24	8.99	6.98	4.80	6.18	106.68	0.42	1.25	1.61
24	Saddle dolomite cement	6.45	4.39	6.25	6.85	7.97	5.53	10.82	10.64	10.64	10.24	12.07	11.92	10.17	10.67	10.85	135.46	0.38	0.69	0.59
25	Saddle dolomite cement	2.00	2.90	3.42	3.31	3.43	6.58	3.12	2.02	3.35	5.07	3.69	2.84	2.03	1.39	2.21	47.36	0.84	1.07	2.01

204

(1) Matrix dolomites have total REE contents (ΣREE+Y) of 24.24×10^{-9}–75.94×10^{-9} (avg. 46.82×10^{-9}), consistent with the generally low REE contents of carbonate rocks. The light-to-heavy REE ratio (LREE/HREE) ranges from 0.27 to 0.62 (avg. 0.53), indicating relative enrichment in HREE. δCe ranges from 0.07 to 0.95 (avg. 0.58) and is therefore negative, with some samples showing a mild negative anomaly and others a pronounced one. δEu ranges from 0.83 to 1.47 (avg. 1.17), and most samples show slight positive anomalies.

(2) Fibrous dolomite cements have ΣREE+Y of 28.69×10^{-9}–42.53×10^{-9} (avg. 34.29×10^{-9}), comparable to that of the matrix dolomite. LREE/HREE ranges from 0.41 to 0.59 (avg. 0.49), again indicating HREE enrichment. δCe ranges from 0.60 to 1.05 (avg. 0.74) and shows a negative anomaly. δEu ranges from 0.61 to 1.38 (avg. 0.87): most samples are negative, whereas a few show pronounced positive anomalies.

(3) Foliated dolomite cements have ΣREE+Y of 81.19×10^{-9}–97.45×10^{-9} (avg. 87.05×10^{-9}), higher than that of the matrix dolomite. LREE/HREE ranges from 0.27 to 0.33 (avg. 0.30), indicating stronger HREE enrichment than in the matrix dolomite. δCe ranges from 0.28 to 0.33 (avg. 0.30) and shows a clear negative anomaly. δEu ranges from 0.94 to 1.24 (avg. 1.06): most samples show no anomaly to a slight positive anomaly.

(4) Fine-crystalline dolomite cements have ΣREE+Y of 14.59×10^{-9}–21.90×10^{-9} (avg. 17.71×10^{-9}), the lowest of all dolomite types. LREE/HREE ranges from 0.46 to 1.01 (avg. 0.63), indicating relative HREE enrichment. δCe ranges from 0.89 to 1.01 (avg. 0.92), corresponding to a slight or negligible negative anomaly. δEu ranges from 1.20 to 1.21 (avg. 1.20) and shows a pronounced positive anomaly.

(5) Medium-crystalline dolomite cements have ΣREE+Y of 116.91×10^{-9}–364.16×10^{-9} (avg. 231.75×10^{-9}), a marked increase relative to the earlier cements. LREE/HREE ranges from 0.20 to 0.55 (avg. 0.34), indicating relative HREE enrichment. δCe ranges from 0.95 to 1.16 (avg. 1.01), with most samples showing no anomaly to a slight positive anomaly. δEu ranges from 0.59 to 0.86 (avg. 0.73) and shows a negative anomaly.

(6) Saddle dolomites have ΣREE+Y of 47.36×10^{-9}–135.46×10^{-9} (avg. 103.98×10^{-9}), higher than that of the matrix dolomite. LREE/HREE ranges from 0.38 to 0.84 (avg. 0.54), indicating relative HREE enrichment. δCe ranges from 0.69 to 1.31 (avg. 1.08), with half of the samples showing slight positive anomalies and the others slight negative anomalies. δEu ranges from 0.59 to 2.01 (avg. 1.45), and several samples display pronounced positive anomalies.

4.3 Carbon and oxygen isotopes

The carbon and oxygen isotope compositions of matrix dolomite and of the different generations of dolomite cement are shown in Fig. 4 and listed in Table 2.

(1) Matrix dolomites have $\delta^{13}C$ values of –0.177‰ to +1.710‰ (avg. +0.815‰) and $\delta^{18}O$ values of –6.306‰ to –4.211‰ (avg. –5.676‰; n = 9). The corresponding powder samples give $\delta^{13}C$ of +0.720‰ to +2.757‰ (avg. +1.522‰) and $\delta^{18}O$ of –5.996‰ to –5.782‰ (avg. –5.886‰; n = 6). The powder results overlap with the laser-ablation values within their combined ranges, supporting the reliability of the in situ data.

(2) Fibrous dolomite cements have $\delta^{13}C$ of +1.355‰ to +2.144‰ (avg. +1.635‰; n = 4) and $\delta^{18}O$ of –5.421‰ to –5.007‰ (avg. –5.169‰; n = 4), similar to the matrix dolomite.

(3) Foliated dolomite cements have $\delta^{13}C$ of +0.259‰ to +0.295‰ (avg. +0.277‰; n = 2) and $\delta^{18}O$ of –7.396‰ to –7.200‰ (avg. –7.298‰; n = 2).

(4) Fine-crystalline dolomite cements have $\delta^{13}C$ of +1.087‰ to +2.547‰ (avg. +1.943‰; n = 6) and $\delta^{18}O$ of –7.709‰ to –6.698‰ (avg. –7.160‰; n = 6).

(5) Medium-crystalline dolomite cements have $\delta^{13}C$ of +1.302‰ to +1.974‰ (avg. +1.564‰; n = 3) and $\delta^{18}O$ of –8.552‰ to –8.109‰ (avg. –8.388‰; n = 3).

(6) Saddle dolomites have $\delta^{13}C$ of –0.255‰ to +1.897‰ (avg. +0.633‰; n = 4) and markedly negative $\delta^{18}O$ of –10.839‰ to –9.933‰ (avg. –10.288‰; n = 4).

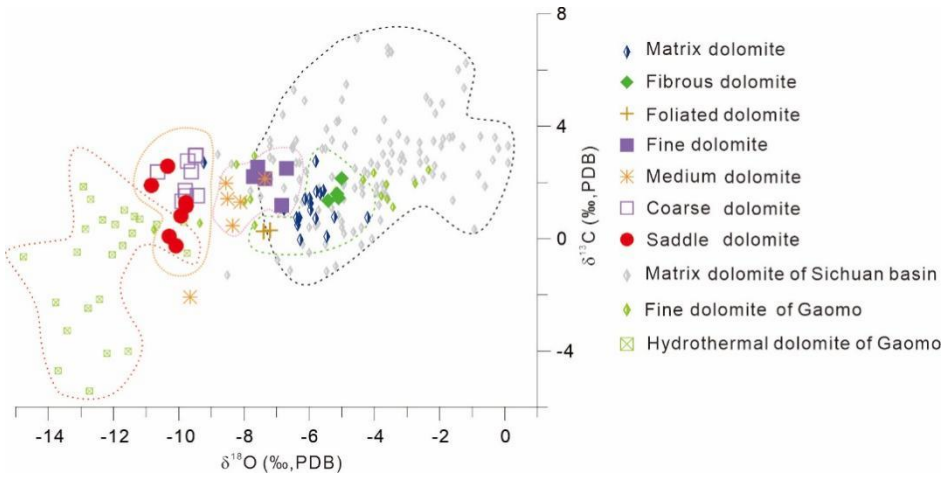


Fig. 4 Carbon and oxygen isotope compositions of matrix dolomite and dolomite cements of the Ediacaran Dengying Formation.

Table 2 Carbon and oxygen isotope compositions of matrix dolomite and dolomite cements of the Ediacaran Dengying Formation

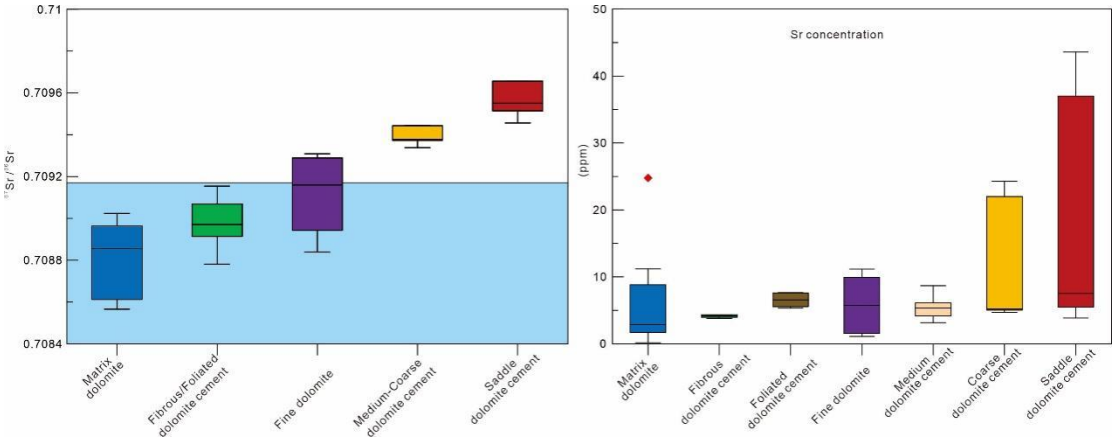
Sample No.	Rock type	$\delta^{13}C$ (‰)	$\delta^{18}O$ (‰)
1	Matrix dolomite	1.407	-6.13
2	Matrix dolomite	0.075	-5.461
3	Matrix dolomite	1.606	-5.66
4	Matrix dolomite	1.71	-5.563
5	Matrix dolomite	0.774	-5.231
6	Matrix dolomite	0.752	-4.211
7	Matrix dolomite	0.557	-6.306
8	Matrix dolomite	0.632	-6.296
9	Matrix dolomite	-0.177	-6.229
10	Matrix dolomite powder	2.757	-5.8
11	Matrix dolomite powder	0.72	-5.802
12	Matrix dolomite powder	1.678	-5.782
13	Matrix dolomite powder	1.172	-5.95
14	Matrix dolomite powder	1.539	-5.996
15	Matrix dolomite powder	1.268	-5.989
16	Fibrous dolomite cement	2.144	-5.007
17	Fibrous dolomite cement	1.597	-5.148
18	Fibrous dolomite cement	1.355	-5.421
19	Fibrous dolomite cement	1.443	-5.102
20	Foliated dolomite cement	0.259	-7.396
21	Foliated dolomite cement	0.295	-7.2
22	Fine-crystalline dolomite cement	2.13	-7.359
23	Fine-crystalline dolomite cement	1.183	-6.845

24	Fine-crystalline dolomite cement	1.087	-6.773
25	Fine-crystalline dolomite cement	2.208	-7.709
26	Fine-crystalline dolomite cement	2.547	-7.579
27	Fine-crystalline dolomite cement	2.501	-6.698
28	Medium-crystalline dolomite cement	1.302	-8.109
29	Medium-crystalline dolomite cement	1.416	-8.503
30	Medium-crystalline dolomite cement	1.974	-8.552
31	Saddle dolomite cement	0.811	-9.933
32	Saddle dolomite cement	0.079	-10.293
33	Saddle dolomite cement	-0.255	-10.086
34	Saddle dolomite cement	1.897	-10.839

265

266 *4.4 Sr isotopes*

267 In this study a total of 20 dolomite samples were selected from the fourth member
268 of the Dengying Formation in the northern Sichuan Basin, and their Sr isotope
269 compositions are reported as $^{87}Sr/^{86}Sr$ ratios (Fig. 5, Table 3).



270

271 Fig. 5 (a) Strontium isotope ($^{87}Sr/^{86}Sr$) ratios of the Ediacaran Dengying Formation
272 dolomite in the Sichuan Basin; coeval seawater ratios (0.7084–0.7095) are from
273 Halverson et al. (2010); (b) Box plot showing the Sr concentration distribution of
274 matrix dolomite and dolomite cements in the Dengying Formation.

275 Table 3 Sr isotopic ratios of the Ediacaran Dengying Formation dolomite in the

Sichuan Basin

Sample No.	Rock type	$^{87}Sr/^{86}Sr$	2σ
1	Matrix dolomite	0.708844911	0.000015
2	Matrix dolomite	0.708612859	0.000015
3	Matrix dolomite	0.708565849	0.000015
4	Matrix dolomite	0.708835909	0.000014
5	Matrix dolomite	0.708896923	0.00001
6	Fibrous–foliated dolomite cement	0.708949935	0.000024
7	Fibrous–foliated dolomite cement	0.708780897	0.000027
8	Fibrous–foliated dolomite cement	0.70915398	0.000013
9	Fine-crystalline dolomite cement	0.70883891	0.000015
10	Fine-crystalline dolomite cement	0.708991944	0.000014
11	Fine-crystalline dolomite cement	0.708942933	0.00002
12	Medium-crystalline dolomite cement	0.708913927	0.000011
13	Medium-crystalline dolomite cement	0.709068961	0.000013
14	Medium-crystalline dolomite cement	0.709038954	0.000015
15	Medium-crystalline dolomite cement	0.709373029	0.000012
16	Saddle dolomite cement	0.709572073	0.000014
17	Saddle dolomite cement	0.70951406	0.000011
18	Saddle dolomite cement	0.709551068	0.000015
19	Saddle dolomite cement	0.709656092	0.000014
20	Saddle dolomite cement	0.709456047	0.000014

(1) The $^{87}Sr/^{86}Sr$ ratios of the matrix dolomites range from 0.708566 to 0.708897, with an average value of 0.708751 (N=5).

(2) The $^{87}Sr/^{86}Sr$ ratios of the fibrous–foliated dolomites range from 0.708781 to 0.709154, with an average value of 0.708962 (N=3).

(3) The $^{87}Sr/^{86}Sr$ ratios of fine-crystalline dolomites range from 0.708839 to 0.708992, with an average value of 0.708925 (N=3).

(4) The $^{87}Sr/^{86}Sr$ ratios of medium-crystalline dolomites range from 0.708914 to 0.709373, with an average value of 0.709099 (N=4).

(5) The $^{87}Sr/^{86}Sr$ ratios of the saddle dolomites range from 0.709456 to 0.709656, with an average value of 0.709550 (N=5), indicating an anomalously high $^{87}Sr/^{86}Sr$ ratio.

4.5 Fluid inclusions

Matrix dolomite was unsuitable for thermometry because the crystals are too small. The fibrous and foliated cements contain mainly single-phase inclusions, and no clear two-phase gas–liquid inclusions were observed (Fig. 6a), so no thermometric data were obtained. Fine-crystalline dolomite contains two-phase gas–liquid brine inclusions together with hydrocarbon inclusions; the latter fluoresce yellow–green (Fig. 6b), and their homogenization temperatures range from 51 to 78 °C (avg. 62 °C). Medium-crystalline dolomite contains mainly two-phase gas–liquid brine inclusions that do not fluoresce (Fig. 6c), with homogenization temperatures of 82–142 °C (avg. 102 °C). Saddle dolomite contains both two-phase gas–liquid brine inclusions and two-phase gas–liquid hydrocarbon inclusions, the latter fluorescing blue–green (Fig. 6d, e); the homogenization temperatures range from 168 to 233 °C (avg. 189 °C). Quartz contains mainly non-fluorescent two-phase gas–liquid brine inclusions (Fig. 6f), with homogenization temperatures of 165–210 °C (avg. 183 °C).

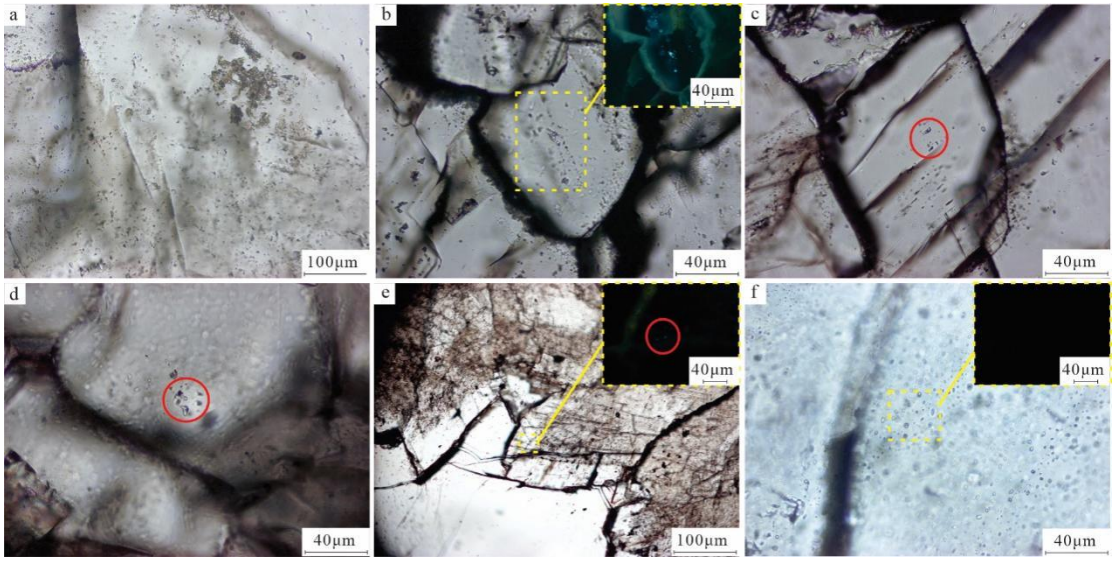


Fig. 6 Fluid inclusion characteristics of the Dengying dolomite reservoirs in the study area.

(a) Single-phase brine inclusions in foliated dolomite cement; (b) gas–liquid two-phase hydrocarbon inclusions in fine-crystalline dolomite cement, which glow yellow–green under fluorescence; (c) medium-crystalline dolomite cement; (d) gas–liquid two-phase brine inclusions in saddle dolomite cement; (e) gas–liquid two-phase hydrocarbon inclusions in saddle dolomite, emitting blue–green light under

fluorescence; and (f) gas–liquid two-phase brine inclusions in quartz do not emit light under fluorescence.

5. Discussion

5.1 Geochemical constraints on diverse fluids in dolomitization

The Dengying Formation in the Sichuan Basin contains seven dolomite types, each reflecting a specific dolomitizing fluid and diagenetic environment. Integrating cathodoluminescence textures with trace elements, C–O–Sr isotopes, REE patterns and fluid inclusion microthermometry, four diagenetic stages are distinguished: (I) penecontemporaneous–early diagenesis in an evaporative marine environment; (II) shallow burial diagenesis; (III) medium-to-deep burial diagenesis; and (IV) tectonic–hydrothermal diagenesis. The following sections evaluate the fluid properties and origins of each stage in turn.

5.1.1 Penecontemporaneous–early diagenesis in an evaporative marine environment

In this environment the sedimentary matrix dolomite underwent early marine cementation, producing fibrous rim and foliated cements. Such cements typically form from aragonite or high-Mg calcite through early dolomitization (Qiang et al. 2017). Micritization, a widespread process in the marine diagenetic realm, is observed in the grains (Fig. 7a, b). Dolomite is particularly abundant in Precambrian successions, where dolomitization tends to occur early (Tucker 1982), and the Dengying Formation, like other Precambrian dolomite units, has been effectively preserved. During Dengying deposition the Sichuan Basin experienced an arid, hot climate with high salinity, and evaporitic sulphate minerals are developed in the basin (Wang et al. 2013; Qiang et al. 2017; Jin et al. 2019). Birdseye structures and tepee structures formed by subaerial exposure indicate that these dolomites formed in the penecontemporaneous to early diagenetic stage, in an evaporative marine setting. The micrite envelopes, matrix dolomite, fibrous rim dolomite and foliated dolomite are non-luminescent to very dull under cathodoluminescence (Fig. 7c), a characteristic of cements precipitated from unmodified seawater (Huang 2010).

Shi et al. (2013) considered that fibrous rim and foliated cements form in different diagenetic environments. Blade-like cement commonly has low Sr and high Fe and Mn contents. The Mn and Fe contents of dolomite reflect the intensity of diagenesis and burial depth, so that deeper burial corresponds to stronger diagenesis and higher Mn and Fe contents (Tucker and Wright 1990). The trace elements of the matrix generally record the geochemical properties of coeval seawater. Both the fibrous rim and the foliated cement show low Fe and Mn contents (<200 ppm; Kaufman et al. 1997). Notably, the foliated cement has the lowest Mn content of all dolomite types (average 4.93 ppm), consistent with precipitation from oxidizing marine pore fluids. These cements formed in the seawater-phreatic zone and are early seafloor cements that lack cathodoluminescence or show very dim cathodoluminescence, which is typical of marine cements.

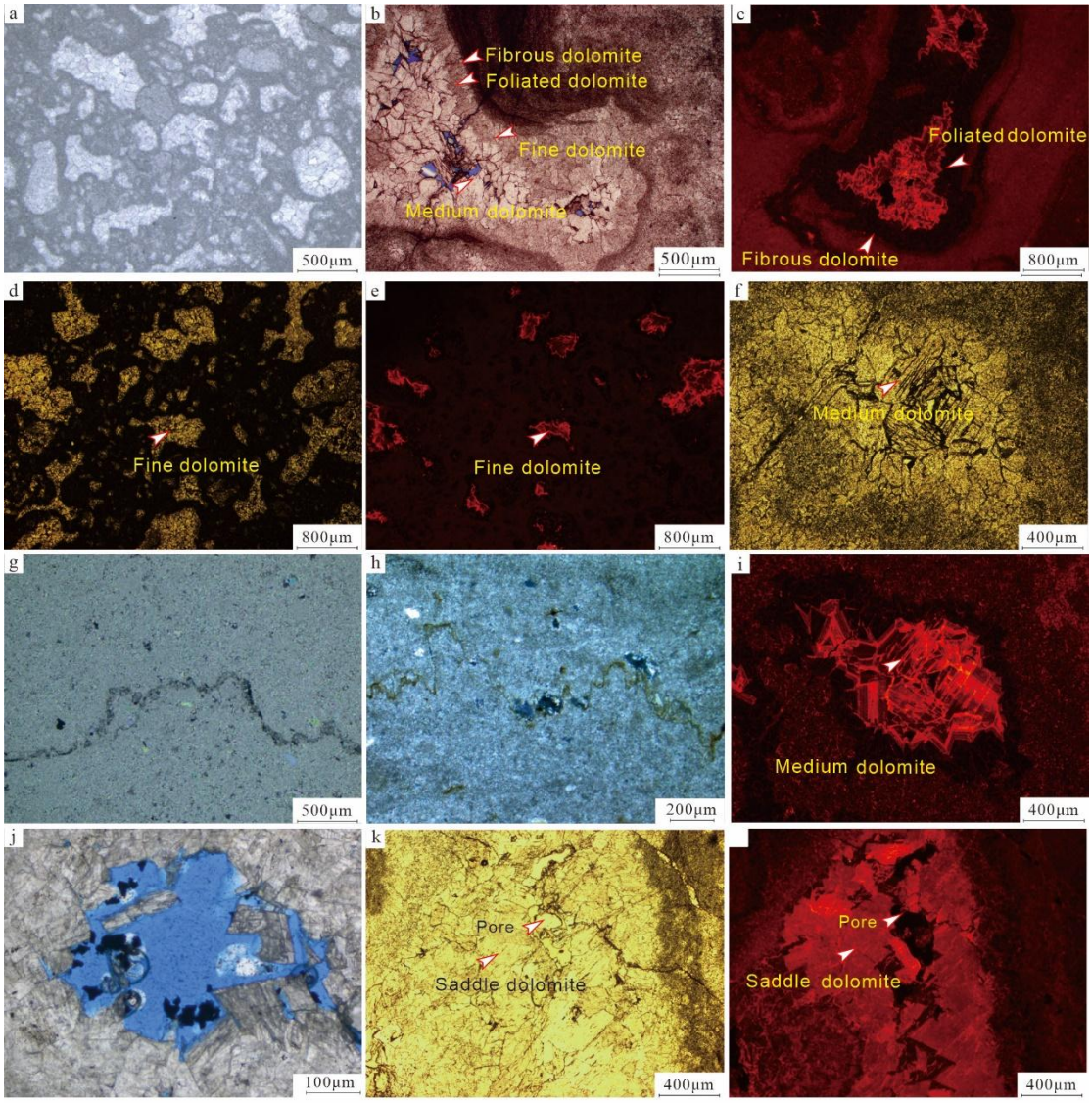


Fig. 7 Thin-section and cathodoluminescence photomicrographs of matrix dolomite and dolomite cements of the Dengying Formation.

(a) Micritization of clotted micrite, plane-polarized light; (b) fibrous and blade-like cements in fine-grained to medium-crystalline dolomite; (c) same field of view as (b), fibrous and foliated dolomite cements; (d) fine-grained dolomite cement, plane-polarized light; (e) same field of view as (d), cathodoluminescence of the fine-crystalline dolomite cement; (f) medium-crystalline dolomite cement, plane-polarized light; (g) same field of view as (f), cathodoluminescence of the medium-crystalline dolomite cement; (h) and (i) stylolite seams developed in matrix dolomite, cross-polarized light; (j) dissolution pores and dolomite cement with flat crystal faces; (k) saddle dolomite, plane-polarized light; (l) same field of view as (k),

cathodoluminescence of the saddle dolomite.

On the $\delta^{13}C$–$\delta^{18}O$ plot (Fig. 4) the matrix dolomite falls within the field of Ediacaran seawater defined by Jaffrés et al. (2007) and Halverson et al. (2010). The fibrous rim and foliated cements show similar C–O isotope compositions, indicating that seawater-derived fluids dominated dolomitization. The $\delta^{18}O$ values of some matrix dolomite and of the cements of the first two stages are slightly higher than those of coeval seawater. This slight enrichment is attributed to evaporation in a restricted setting, where microbial activity continuously removed Ca^{2+} and concentrated Mg^{2+} (Qiang et al. 2017; Jin et al. 2019; Jiang et al. 2022). Normal seawater thus evolved progressively into a high-Mg brine that reacted with the earlier aragonite or high-Mg calcite, driving evaporative–reflux dolomitization.

Strontium isotopes confirm that the matrix, fibrous rim and foliated dolomites formed in a marine environment. Their $^{87}Sr/^{86}Sr$ ratios coincide with the composition of Ediacaran seawater (Fig. 5; Shields and Veizer 2002; Halverson et al. 2010), and the values obtained for the fibrous–foliated cements fall within the coeval seawater range, indicating that the diagenetic fluid remained seawater and was not affected by external fluids.

The PAAS-normalized REE patterns of matrix dolomite show two forms (Fig. 3a). One has a strong negative δCe anomaly together with a pronounced positive Y anomaly, resembling the pattern of seawater; its relatively high δCe is comparable to that of Cambrian–Ordovician carbonates in the Tarim Basin, and a similar Ce signature in sabkha dolomite has been attributed to evaporation (Zhao et al. 2012). The other pattern is nearly flat with no obvious δCe anomaly, indicating that REEs did not migrate significantly during dolomitization, consistent with the reflux model. In that model the slightly positive δEu anomaly indicates that the matrix dolomite formed in the evaporative–reflux environment was later overprinted by hydrothermal fluids. Microscopically, the fibrous and foliated cements contain mainly single-phase inclusions with no clear two-phase gas–liquid inclusions (Fig. 6a), suggesting precipitation from a low-temperature homogeneous liquid at an early diagenetic stage

(Fig. 8).

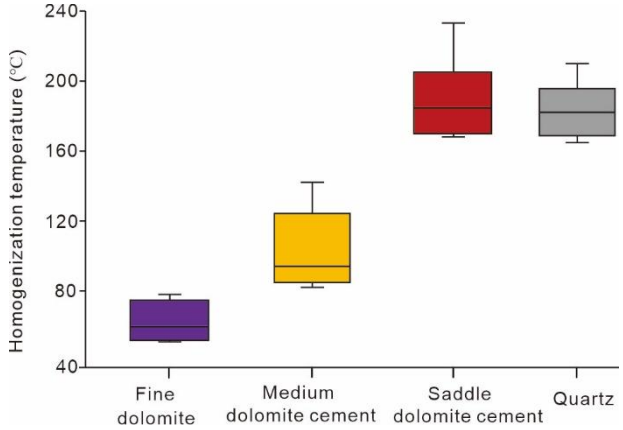


Fig. 8 Box plot of fluid inclusion homogenization temperatures of the Ediacaran Dengying Formation dolomites.

5.1.2 Shallow burial diagenesis

In the shallow burial environment, fine-crystalline dolomite cement developed and shows moderate orange–red cathodoluminescence (Fig. 7d, e). The increase in Mn and Fe contents indicates that this cement formed in a reducing environment. The C–O isotope compositions of the fine-crystalline cement lie mostly within the range of coeval seawater (Fig. 4), whereas some samples have $\delta^{18}O$ values slightly below it. Because the oxygen isotope values of carbonate are sensitive to fluid temperature (Swart 2015), increasing burial depth and pore-fluid temperature drive ^{18}O depletion, so the observed shift implies a certain burial depth. The $^{87}Sr/^{86}Sr$ ratios remain within the range of Ediacaran seawater, indicating that the diagenetic fluid was not affected by foreign fluids and still recorded original seawater (Fig. 5a). The REE pattern of the fine-crystalline cement shows a negative δCe anomaly and a pronounced positive Y anomaly (Fig. 3d), essentially reproducing the signature of concentrated seawater. Hydrocarbon inclusions in this cement fluoresce yellow–green (Fig. 6b), reflecting a low degree of thermal maturity of the organic matter. Its homogenization temperature (51–78 °C) is slightly higher than the Ediacaran palaeo-seawater temperature (7–38.6 °C), indicating that the fine-crystalline dolomite precipitated from seawater stored in the formation during earlier diagenesis (Fig. 8).

5.1.3 Medium-to-deep burial diagenesis

Burial-precipitated dolomites form once the pore fluids become sufficiently alkaline, which favours carbonate saturation or supersaturation. In the medium-to-deep burial environment, well-crystallized medium-crystalline dolomite cement precipitated (Fig. 7f), locally accompanied by stylolites (Fig. 7h). Under cathodoluminescence this cement shows strong orange–red luminescence (Fig. 7g), indicating greater burial depth and a more reducing diagenetic environment. Its $\delta^{13}C$ values are little changed from those of the fine-crystalline cement, whereas $\delta^{18}O$ is more negative (Fig. 4), again indicating deeper burial. The $^{87}Sr/^{86}Sr$ ratios of the medium-crystalline dolomite confirm a medium-to-deep burial setting (Fig. 5a). These ratios are generally higher than coeval seawater values, reaching a maximum of 0.709373, which indicates that the fluid had interacted with ancient crustal rocks carrying radiogenic Sr. The REE pattern shows pronounced HREE enrichment, with δCe values close to unity (avg. 1.01). During burial, rising temperature and increasingly reducing conditions reduced Ce^{4+} to the more soluble Ce^{3+}, thereby weakening the negative Ce anomaly. The REE distribution resembles that of pore water (Fig. 3e), pointing to a burial dolomitization origin. Two-phase gas–liquid brine inclusions are common in the medium-crystalline cement, indicating that the cement formed before the second stage of hydrocarbon charging (Fig. 6c). Their homogenization temperatures (82–142 °C) indicate burial depths greater than those of the fine-crystalline dolomite (Fig. 8).

Coarse-crystalline dolomite occurs as cement in secondary dissolution pores and vugs (Fig. 7j). Its Sr content is the highest among the burial cements, whereas its Mn and Fe contents are comparable to those of the medium-crystalline cement. These features indicate precipitation from reduced pore waters at burial depths similar to, or slightly greater than, those of the medium-crystalline cement, with only limited interaction with radiogenic crustal fluids.

5.1.4 Tectonic–hydrothermal diagenesis

Saddle dolomite shows strong, bright red cathodoluminescence, and its $\delta^{18}O$ values are almost all below –10‰ (Fig. 4), indicating strong diagenetic modification (Kaufman and Knoll 1995). Feng et al. (2017) and Su et al. (2022) reported comparable

results for hydrothermal dolomite in central Sichuan. The anomalously high $^{87}Sr/^{86}Sr$ ratios confirm that the saddle dolomite fluid was influenced by radiogenic Sr derived from ancient aluminosilicate crust (Fig. 5a). In the northern margin of the Sichuan Basin the strata beneath the Dengying Formation contain granite intrusions, and beneath these intrusions lie Nanhua sandy clastic rocks; in some areas the base of the Dengying Formation rests directly on basement volcanic rocks (Yang et al. 2019). These clastic units are the likely source of the radiogenic Sr. The REE pattern of saddle dolomite shows a pronounced positive δEu anomaly (Fig. 3f), indicating a significant hydrothermal influence on the dolomitization of the fourth member. Two inclusion types, two-phase gas–liquid brine and two-phase gas–liquid hydrocarbon (Fig. 6d, e), are common in saddle dolomite. The hydrocarbon inclusions fluoresce blue–green, with homogenization temperatures of 168–233 °C (avg. 189 °C). Quartz contains mainly non-fluorescent two-phase gas–liquid brine inclusions (Fig. 6f), with homogenization temperatures of 165–210 °C (avg. 183 °C). The fluorescence colour of hydrocarbon inclusions reflects the composition and thermal maturity of the organic matter (Liu et al. 2013): with increasing maturity the aromatic fraction of the charged crude oil decreases and the fluorescence shifts to shorter wavelengths. The change from yellow–green fluorescence in the fine-crystalline cement to blue–green fluorescence in saddle dolomite therefore indicates increasing thermal maturity of the source rocks. Overall, homogenization temperatures increase from the fine-crystalline cement through the medium-crystalline cement to saddle dolomite and quartz.

5.2 Carbonate diagenesis and reservoir quality

Dolomite-hosted reservoirs are the main type of high-quality reservoir in the Dengying Formation of the Sichuan Basin. Because the pore network of these dolomites was inherited from the precursor sediment, dolomitization itself added little new porosity. Early dolomitization nevertheless increased the resistance of the rock to compaction and pressure solution, favouring the preservation of pre-existing pores (Shen et al. 2015, 2022). The initial porosity of the precursor and the dolomitization pathway were therefore the main controls on reservoir development (Qiao et al. 2022). During Dengying deposition the region had an arid, hot palaeoclimate and evaporation

in the basin was intense (Zhang et al. 2004); bacteria and algae flourishing in the Dengying Formation continuously consumed Ca^{2+} and concentrated Mg^{2+}, so that normal seawater evolved into high-Mg brine. Reflux dolomitization of evaporated seawater, mediated by microbial activity, was thus the main dolomitization mechanism. The microbial mound-shoal complexes at the platform margin and within the platform consist of microbial and grain dolomite deposited under strong hydrodynamic conditions, and had relatively high initial porosity and permeability, making them the main reservoir rocks in the study area (Grotzinger and Al-Rawahi 2014). Although most primary pores and cavities were later filled by dolomite cement, the dolomitized framework is inferred to have retained relatively good porosity and permeability, allowing various acidic fluids to migrate during late diagenesis and to create further secondary pores and cavities.

Dissolution pores and karst caves are well developed in the mound-shoal belt at the platform margin, where exploration results are encouraging. The microbial mounds and shoals of the Dengying Formation formed under strong hydrodynamic conditions. Clotted fabrics and early diagenetic dolomitization of the stromatolites made the rock resistant to compaction, providing the material basis for reservoir development and favouring later diagenetic modification.

Hydrothermally altered dolomite forms a second type of high-quality reservoir, as documented in the Gaomo area of the Sichuan Basin (Jiang et al. 2016; Feng et al. 2017). During the Neoproterozoic to Early Cambrian, in the extensional regime that followed the breakup of Rodinia (Wang and Li 2003), continental rifts developed in the basin and the Deyang–Anyue rift trough formed. Rifting controlled the Ediacaran–Early Cambrian palaeogeography of the Sichuan Basin, with alternating troughs and highs that were elevated in the west and low in the east during Dengying deposition (Wen et al. 2021). The basin subsequently experienced multiple tectonic cycles (He et al. 2011). From the late Permian to the Early Triassic, strong crustal extension produced faults and fractures, and seismic interpretation shows that high-angle faults developed across the area (Hou et al. 2017; Zhao et al. 2017). These basement faults remained active and acted as conduits for hydrothermal fluids, which is why hydrothermal alteration locally

enhanced reservoir quality in the Gaomo area (Jiang et al. 2016; Feng et al. 2017).

5.3 A facies–diagenesis–fluid model for reservoir development

Sedimentary facies set the initial framework. Microbial mound-shoal complexes at the platform margin and within the platform accumulated microbial and grain dolomite with high primary porosity and permeability, and this primary pore network persisted because early dolomitization increased the resistance of the rock to compaction and pressure solution (Shen et al. 2015, 2022; Qiao et al. 2022). Facies therefore determine where reservoir space could develop in the first place.

Early diagenesis determined how much of that space survived. Reflux dolomitization of evaporated seawater, mediated by microbial consumption of calcium and concentration of magnesium, produced the matrix dolomite and the fibrous and foliated cements. Subsequent cementation reduced porosity, but the dolomitized framework remained sufficiently connected to allow later acidic fluids to pass, so that secondary dissolution pores and vugs could develop.

Fluid activity determined the final distribution of enhanced porosity. Burial formation waters, and more importantly tectonically driven hydrothermal fluids, selectively enlarged pores along fault and fracture zones, as recorded by saddle dolomite with strongly negative oxygen isotope values (below –10‰), elevated strontium isotope ratios and positive Eu anomalies. The coincidence of favourable facies, preservative early dolomitization and late fluid flux explains the distribution of high-quality reservoirs in the study area.

This study did not measure porosity or permeability, so the model proposed here is genetic and qualitative rather than quantitatively predictive. Calibrating the relative contribution of each element will require core-plug porosity and permeability data measured across the diagenetic stages identified above.

6. Conclusions

The Dengying Formation of the Sichuan Basin contains a variety of dolomite types, and their differences record the relationships between dolomitizing fluids and formation environments. Matrix dolomite and the early seawater cements, that is the fibrous rim and foliated dolomite, precipitated in an evaporative marine environment, whereas the

fine- to coarse-crystalline dolomites formed during progressive burial, and the saddle dolomite precipitated from tectonically driven hydrothermal fluids.

Microbialite-associated early dolomitization provides the primary framework for high-quality reservoirs in the northern Sichuan Basin. The initial porosity of precursor sediments and the early dolomitization pathway are the first-order controls on reservoir development. In contrast, tectonically driven hydrothermal alteration, transmitted along basement faults reactivated during late Permian to Early Triassic extension, locally enhances reservoir quality, as documented in the Gaomo area; this overprint is secondary but locally significant.

Under favourable palaeogeographic and facies control, the prerequisites for high-quality reservoir development were early dolomitization together with the primary framework pores of microbial mounds and the intergranular pores of grainstones. Late diagenesis then exerted an important influence on reservoir quality. Reservoir development in these deeply buried dolomites follows a facies–diagenesis–fluid framework in which favourable microbial mound-shoal facies, preservative early dolomitization and late burial to hydrothermal fluid flux act together, as set out in Section 5.3.

Statements and Declarations

Funding: This work was supported by the Scientific and Technology Project of PetroChina (No.: 2026DJ010 and 2023ZZ0201), the National Natural Science Foundation of China (U23B200575) and the Science and Technology Project of Sichuan Province (2022YFS0466). The funding sources had no role in the design of the study; in the collection, analysis or interpretation of data; in the writing of the report; or in the decision to submit the article for publication.

Competing interests: The authors declare that they have no known competing financial interests or personal relationships that could have appeared to influence the work reported in this paper.

Data availability: All data generated or analysed during this study are included in this

published article.

Author contributions: All authors contributed to the study conception and design. Material preparation, data collection and analysis were performed by Li Qiufen, Tan Cong, Wang Tongshan, Du Qiuding, Gu Zhidong, Shi Shuyuan and Zhai Xiufen. The first draft of the manuscript was written by Li Qiufen and Tan Cong, and all authors commented on previous versions of the manuscript. All authors read and approved the final manuscript.

References

Bjørlykke K, Jahren J (2012) Open or closed geochemical systems during diagenesis in sedimentary basins: constraints on mass transfer during diagenesis and the prediction of porosity in sandstone and carbonate reservoirs. AAPG Bull 96: 2193–2214

Cai CF, He WX, Jiang L, Li KK, Xiang L, Jia LQ (2014) Petrological and geochemical constraints on porosity difference between Lower Triassic sour- and sweet-gas carbonate reservoirs in the Sichuan Basin. Mar Pet Geol 56: 34–50

Deng SH, Fan R, Li X, Zhang SB, Zhang BM, Lu YZ (2015) Subdivision and correlation of the Sinian (Ediacaran) system in the Sichuan Basin and its adjacent area. J Stratigr 39: 239–254 (in Chinese)

Ding Y, Li ZW, Liu SG, Song JM, Zhou XQ, Sun W, Zhang XH, Li SJ, Ran B, Peng HL, Li ZQ, Wan H, Chen DZ (2021) Sequence stratigraphy and tectono-depositional evolution of a late Ediacaran epeiric platform in the upper Yangtze area, South China. Precambrian Res 354: 1–24

Du JH, Zou CN, Xu CC, He HQ, Shen P, Yang YM, Li YL, Wei GQ, Wang ZC, Yang Y (2014) Theoretical and technical innovations in strategic discovery of a giant gas field in Cambrian Longwangmiao Formation of central Sichuan paleo-uplift, Sichuan Basin. Pet Explor Dev 41: 294–305

Du JH, Wang ZC, Zou CN, Xu CC, Shen P, Zhang BM, Jiang H, Huang SP (2016) Discovery of intra-cratonic rift in the Upper Yangtze and its control effect on the formation of Anyue giant gas field. Acta Pet Sin 37: 1–16 (in Chinese)

Feng MY, Wu PC, Qiang ZT, Liu XH, Duan Y, Xia ML (2017) Hydrothermal

dolomite reservoir in the Precambrian Dengying Formation of central Sichuan Basin, southwestern China. Mar Pet Geol 82: 206–219

Grotzinger J, Al-Rawahi Z (2014) Depositional facies and platform architecture of microbialite-dominated carbonate reservoirs, Ediacaran–Cambrian Ara Group, Sultanate of Oman. AAPG Bull 98: 1453–1494

Halverson GP, Wade BP, Hurtgen MT, Barovich KM (2010) Neoproterozoic chemostratigraphy. Precambrian Res 182: 337–350

Han JF, Wang P, Zhu GY, Zhang YT, Li SY, Xie Z (2023) Petroleum geology and distribution law of high efficiency areas in ultra-deep kiloton wells in Tarim Basin. Nat Gas Geosci 34: 735–748

He DF, Zhang DS, Zhang GW, Zhao LZ, Fan C, Lu RQ, Wen Z (2011) Formation and evolution of multi-cycle superposed Sichuan Basin, China. Sci Geol Sin 3: 589–606 (in Chinese)

Hou MC, Xing FC, Xu SL, Lin LB, Liu XC, Xiong FH, Huang H (2017) Paleogeographic patterns of E–C transition period in the upper Yangtze and the geodynamic mechanism. Acta Sedimentol Sin 5: 902–917 (in Chinese)

Huang SJ (2010) Carbonate Diagenesis. Geological Publishing House, Beijing

Jaffrés JBD, Shields GA, Wallmann K (2007) The oxygen isotope evolution of seawater: a critical review of a long-standing controversy and an improved geological water cycle model for the past 3.4 billion years. Earth-Sci Rev 83: 83–122

Javanbakht M, Wanas HA, Jafarian A, Shahsavan N, Sahraeyan M (2018) Carbonate diagenesis in the Barremian–Aptian Tirgan Formation (Kopet-Dagh Basin, NE Iran): petrographic, geochemical and reservoir quality constraints. J Afr Earth Sci 144: 122–135

Jia CZ, Zhang SC (2023) The formation of marine ultra-deep petroleum in China. Acta Geol Sin 9: 2775–2801

Jiang L, Worden RH, Cai CF, Shen AJ, Crowley SF (2018) Diagenesis of an evaporite-related carbonate reservoir in deeply buried Cambrian strata, Tarim Basin, northwest China. AAPG Bull 102: 77–102

624 Jiang L, Shen AJ, Wang ZC, Hu AP, Wang YS, Luo XY, Liang F, Azmy K, Pan LY
625 (2022) U–Pb geochronology and clumped isotope thermometry study of
626 Neoproterozoic dolomites from China. Sedimentology 69: 2925–2945
627 Jiang YQ, Tao YZ, Gu YF, Wang JB, Qiang ZT, Jiang N, Lin G, Jiang C (2016)
628 Hydrothermal dolomitization in Dengying Formation, Gaoshiti–Moxi area,
629 Sichuan Basin, SW China. Pet Explor Dev 43: 54–64
630 Jin MD, Tan XC, Li BS, Zhu X, Zeng W, Lian CB (2019) Genesis of dolomite in the
631 Sinian Dengying Formation in the Sichuan Basin. Acta Sedimentol Sin 3: 443–
632 454 (in Chinese)
633 Kaufman AJ, Knoll AH (1995) Neoproterozoic variations in the C-isotopic
634 composition of seawater: stratigraphic and biogeochemical implications.
635 Precambrian Res 73: 27–49
636 Kaufman AJ, Knoll AH, Narbonne GM (1997) Isotopes, ice ages, and terminal
637 Proterozoic earth history. Proc Natl Acad Sci 94: 6600–6605
638 Li Y, Wang XZ, Feng MY, Zeng DM, Xie SY, Fan R, Wang LJ, Zeng T, Yang XF
639 (2019) Reservoir characteristics and genetic differences between the second and
640 fourth members of Sinian Dengying Formation in northern Sichuan Basin and its
641 surrounding areas. Pet Explor Dev 46
642 Li ZQ, Liu J, Li Y, Hang WY, Hong HT, Ying DL, Chen X, Liu R, Duan XG, Peng J
643 (2015) Formation and evolution of Weiyuan–Anyue tensional corrosion trough in
644 Sinian system, Sichuan Basin. Pet Explor Dev 12: 29–36
645 Li ZZ, Shi JHC, Wang JH, Liang F (2022) Characteristics of residual hill-type
646 reservoir of Sinian Dengying Formation in Deyang–Anyue ancient rift trough,
647 central Sichuan and its significance for oil and gas exploration. Nat Gas Geosci
648 8: 1263–1275 (in Chinese)
649 Liu BJ, Xu XS (eds) (1994) Atlas of the Lithofacies and Palaeogeography of South
650 China (Sinian–Triassic). Science Press, Beijing
651 Liu KY, Bourdet J, Zhang BS, Zhang N, Lu XS, Liu SB, Pang H, Li Z, Guo XW
652 (2013) Hydrocarbon charge history of the Tazhong Ordovician reservoirs, Tarim
653 Basin as revealed from an integrated fluid inclusion study. Pet Explor Dev 40:

183–193

Liu SG, Yang Y, Deng B, Zhong Y, Wen L, Sun W, Li ZW, Jansa LB, Li JX, Song JM, Zhang XH, Peng HL (2021) Tectonic evolution of the Sichuan Basin, southwest China. Earth-Sci Rev 213: 103470

Luo B, Yang Y, Luo W, Wen L, Wang W, Chen K (2017) Controlling factors of Dengying Formation reservoirs in the central Sichuan paleo-uplift. Pet Res 2: 54–63

Luo ZL (1991) Taphrogenesis and Distribution of Petroleum Deposits in China. Petroleum Industry Press, Beijing (in Chinese)

Ma YS, Guo XS, Guo TL, Huang R, Cai XY, Li GX (2007) The Puguang gas field: new giant discovery in the mature Sichuan Basin, southwest China. AAPG Bull 91: 627–643

Ma YS, Cai XY, Zhao PR, Luo Y, Zhang XF (2010) Distribution and further exploration of the large-medium sized gas fields in Sichuan Basin. Acta Pet Sin 3: 347–354

Ma YS, Cai XY, Yun L, Li ZJ, Li HL, Deng S, Zhao PR (2022) Practice and theoretical and technical progress in exploration and development of Shunbei ultra-deep carbonate oil and gas field, Tarim Basin, NW China. Pet Explor Dev 1: 1–20

Pang XQ, Lin HX, Zheng DY, Li HL, Zou HY, Pang H, Hu T, Guo FX, Li HY (2020) Basic characteristics, dynamic mechanism and development direction of the formation and distribution of deep and ultra-deep carbonate reservoirs in China. J Geomech 5: 673–695

Pourmand A, Dauphas N, Ireland TJ (2012) A novel extraction chromatography and MC-ICP-MS technique for rapid analysis of REE, Sc and Y: revising CI-chondrite and Post-Archean Australian Shale (PAAS) abundances. Chem Geol 291: 38–54

Qiang ST, Shen P, Zhang J, Xia ML, Feng MY, Xia QS, Tao YZ, Xia ZQ, Lin Y (2017) The evolution of carbonate sediment diagenesis and pore fluid in Dengying Formation, central Sichuan Basin. Acta Sedimentol Sin 4: 797–811 (in

684 Chinese)
685 Qiao ZF, Zhang SN, Shen AJ, She M, Huang LL, Li WZ, Shao GM, Dai CR (2022)
686 Controls on formation and development of large-sized high-quality dolomite
687 reservoirs in the Tarim and Sichuan Basins. Oil Gas Geol 43: 92–104
688 Shen AJ, Zhao WZ, Hu AP, She M, Chen YN, Wang XF (2015) Major factors
689 controlling the development of marine carbonate reservoirs. Pet Explor Dev 42:
690 597–608
691 Shen AJ, She M, Hu AP, Pan LY, Lu JM (2016) Scale and distribution of marine
692 carbonate burial dissolution pores. J. Nat Gas Geosci 1: 187–193
693 Shen AJ, Luo XY, Hu AP, Qiao ZF, Zhang J (2022) Dolomitization evolution and its
694 effects on hydrocarbon reservoir formation from penecontemporaneous to deep
695 burial environment. Pet Explor Dev 49: 731–743
696 Shi ZJ, Wang Y, Tian YM, Wang CC (2013) Cementation and diagenetic fluid of algal
697 dolomites in the Sinian Dengying Formation in southeastern Sichuan Basin. Sci
698 China Earth Sci 56: 192–202
699 Shields G, Veizer J (2002) Precambrian marine carbonate isotope database: version
700 1.1. Geochem Geophys Geosyst 3: 1–12
701 Su A, Chen HH, Feng YX, Zhao JX, Wang ZC, Hu MY, Jiang H, Duc Nguyen A
702 (2022) In situ U–Pb dating and geochemical characterization of multi-stage
703 dolomite cementation in the Ediacaran Dengying Formation, Central Sichuan
704 Basin, China: constraints on diagenetic, hydrothermal and paleo-oil filling
705 events. Precambrian Res 368: 106481
706 Swart PK (2015) The geochemistry of carbonate diagenesis: the past, present and
707 future. Sedimentology 62: 1233–1304
708 Tucker ME (1982) Precambrian dolomites: petrographic and isotopic evidence that
709 they differ from Phanerozoic dolomites. Geology 10: 7–12
710 Tucker ME, Wright VP (1990) Carbonate Sedimentology. Blackwell Scientific
711 Publications, Oxford
712 Wang J, Li ZX (2003) History of Neoproterozoic rift basins in South China:
713 implications for Rodinia break-up. Precambrian Res 122: 141–158

714 Wang LC, Liu CL, Zhang H (2013) Tectonic and sedimentary settings of evaporites in
715 the Dengying Formation, South China Block: implications for the potential of
716 potash formation. Acta Geosci Sin 5: 585–593 (in Chinese)
717 Wang LJ (2019) Characteristics and controlling factors of high-quality reservoirs of
718 the fourth member of Dengying Formation in northern Sichuan Basin. Lithol
719 Reserv 2: 35–45 (in Chinese)
720 Wei GQ, Yang W, Du JH, Xu CC, Zou CN, Xie WR, Zeng FY, Wu SJ (2015)
721 Geological characteristics of the Sinian–Early Cambrian intracratonic rift,
722 Sichuan Basin. Nat Gas Ind 35: 24–35
723 Wei GQ, Yang W, Zhang J, Xie WR, Zeng FY, Su N, Jin H (2018) The pre-Sinian rift
724 in central Sichuan Basin and its control on hydrocarbon accumulation in the
725 overlying strata. Pet Explor Dev 45: 179–189
726 Wen L, Luo B, Zhong Y, Ma K, Zhang XH, Li Y, Peng HL, Li KY, Zhou HF (2021)
727 Sedimentary characteristics and genetic model of trough-platform system during
728 the Dengying period in Sichuan Basin, China. J Chengdu Univ Technol (Sci
729 Technol Ed) 48: 513–524 (in Chinese)
730 Yang RQ, Yang FL, Zhou XF, Zhou Z (2019) Paleogeographic evolution of the
731 Dengying Formation in Hannan–northeastern Sichuan Basin: sedimentary
732 evidence of the extensional tectonic setting for the northwest margin of the
733 Yangtze Block in the late Sinian. Acta Sedimentol Sin 1: 189–199 (in Chinese)
734 Yang W, Wei GQ, Xie WR, Su N, Zeng FY, Hao CG, Bai ZZ, Li R, Wu XQ, Su YQ
735 (2022) Main controlling factors and genetic mechanism for the development of
736 high-quality reservoirs in the mound-shoal complexes on the platform margin
737 mound-beach body at platform margin of the inner cratonic rift: case study of the
738 fourth member of Dengying Formation in the east side of the Deyang–Anyue
739 cratonic rifts, Sichuan Basin. Nat Gas Geosci 10: 1541–1553 (in Chinese)
740 Zhang TG, Chu XL, Zhang QR, Feng LJ, Huo WG (2004) The sulfur and carbon
741 isotopic records in carbonates of the Dengying Formation in the Yangtze
742 Platform, China. Acta Petrol Sin 20: 717‐724 (in Chinese)
743 Zhao DF, Tan XC, Luo WJ, Wang XF, Xu W, Luo SC, Tang DH, Luo Y, Zeng W

(2022a) Karst characteristics at early diagenetic stage and their enlightenment for the origin of ancient deep carbonate reservoirs: a case study of the Member 4 of Dengying Formation in Moxi 8 well area, central Sichuan. Acta Pet Sin 9: 1236–1252

Zhao MY, Zheng YF (2017) A geochemical framework for retrieving the linked depositional and diagenetic histories of marine carbonates. Earth Planet Sci Lett 460: 213–221

Zhao WZ, Shen AJ, Hu SY, Zhang BM, Pan WQ, Zhou JG, Wang ZC (2012) Geological conditions and distributional features of large-scale carbonate reservoirs onshore China. Pet Explor Dev 39: 1–14

Zhao WZ, Wei GQ, Yang W, Mo WL, Xie WR, Su N, Liu MC, Zeng FY, Wu SJ (2017) Discovery of Wanyuan–Dazhou intracratonic rift and its significance for gas exploration in Sichuan Basin, SW China. Pet Explor Dev 44: 697–707

Zhao WZ, Wang XF, Wang X, Wang K, Shen AJ (2022b) Stratigraphic sequence re-determination and lithofacies palaeogeographical characteristics of the Sinian Dengying Formation in Sichuan Basin. J Palaeogeogr 24: 852–870

Zhu MY, Zhang JM, Yang AH (2007) Integrated Ediacaran (Sinian) chronostratigraphy of South China. Palaeogeogr Palaeoclimatol Palaeoecol 254: 7–61